

# Electric-Field-Controlled Phase Transformation in WO<sub>3</sub> Thin Films through Hydrogen Evolution

Meng Wang, Shengchun Shen, Jinyang Ni, Nianpeng Lu, Zhuolu Li, Hao-Bo Li, Shuzhen Yang, Tianzhe Chen, Jingwen Guo, Yujia Wang, Hongjun Xiang, and Pu Yu\*

Field-effect transistors with ionic-liquid gating (ILG) have been widely employed and have led to numerous intriguing phenomena in the last decade, due to the associated excellent carrier-density tunability. However, the role of the electrochemical effect during ILG has become a heavily debated topic recently. Herein, using ILG, a field-induced insulator-to-metal transition is achieved in WO<sub>3</sub> thin films with the emergence of structural transformations of the whole films. The subsequent secondary-ion mass spectrometry study provides solid evidence that electrochemically driven hydrogen evolution dominates the discovered electrical and structural transformation through surface absorption and bulk intercalation.

Field effect transistors with the ionic liquid gating (ILG) have been widely employed and led to numerous intriguing phenomena in the last decade.<sup>[1–13]</sup> During the ILG, nanometer spacing charged layer, called electric double layers, forms at the solid/electrolyte interface, which mimics a dielectric capacitor and enables giant carrier modulation with the sheet carrier density up to 10<sup>15</sup> cm<sup>-2</sup>.<sup>[2]</sup> Owing to the excellent carrier density tunability, ILG has demonstrated its unique capability of exploring

various exotic properties in various material systems, such as the insulator-metal transition (IMT),<sup>[2–7]</sup> superconductivity,<sup>[8–12]</sup> and magnetism.<sup>[10,13]</sup> However, recent studies at VO<sub>2</sub> and WO<sub>3</sub> thin films have suggested that oxygen ions evolution driven by electrochemical process can be induced during the ILG, which plays an essential role for the observed IMT and structure deformation.<sup>[14–16]</sup> Furthermore, it has recently been reported that electrochemical protonation can also emerge in VO<sub>2</sub> and SrCoO<sub>2.5</sub> films with the positive biased ILG, which brought another possibility into the heavily debated mechanisms

of the ILG-induced IMT.<sup>[17,18]</sup> Especially, the doping level in protonated SrCoO<sub>2.5</sub> can be as high as one electron per formula unit cell in a thick film,<sup>[18]</sup> which is more than an order of magnitude higher than carrier concentration by electrostatic effects or vacancy concentration with oxygen ion evolution reported before.<sup>[7,16]</sup> Clearly, the higher doping level brings in great possibility to modulate various properties in materials. However, the research for ILG-induced hydrogen evolution (or protonation) is still in its relative infancy, and clearly further studies to extend this approach to a large variety of functional materials will give a big boost to the development of related fields.

WO<sub>3</sub>, a perovskite-type (ABO<sub>3</sub>) crystal with vacant A sites, as shown in Figure 1a, is an excellent model system for the ILG-induced protonation study due to its associated ideal channels for ionic intercalation<sup>[19,20]</sup> and the simple band structure for the electrical transport study. WO<sub>3</sub> is an insulator with unoccupied 5d<sup>0</sup> conduction band and can become metal and even superconductor upon doping with alkali ions.<sup>[19–21]</sup> Its lattice structure is readily changed depending on carrier/dopant density,<sup>[20–22]</sup> which makes the in situ structural characterization a perfect probe to trace the IMT through ILG. In this study, combining both the electrical transport and in situ X-ray diffraction (XRD) measurements, we demonstrated an ILG-induced metallization of the insulating WO<sub>3</sub> films with the positive biased gating as small as 1.5 V. Unexpectedly, when further increasing the gate voltage above 3.5 V, we observed a large continuous structural transformation accompanied with the clearly suppressed electrical conductivity. Furthermore, the ion depth profiles through the secondary ion mass spectrometry (SIMS) measurements provide solid evidence that the hydrogen intercalation was strongly correlated with the observed structural transformation. In contrast to the previously reported ILG-induced metallization in the WO<sub>3</sub> system with small structural

M. Wang, Dr. S. Shen, Dr. N. Lu, Z. Li, Dr. H. Li, S. Yang, T. Chen, J. Guo, Y. Wang, Prof. P. Yu  
State Key Laboratory of Low Dimensional Quantum Physics  
and Department of Physics  
Tsinghua University  
Beijing 100084, China  
E-mail: yupu@mail.tsinghua.edu.cn

J. Ni, Prof. H. Xiang  
Key Laboratory of Computational Physical Sciences  
(Ministry of Education)  
State Key Laboratory of Surface Physics  
and Department of Physics  
Fudan University  
Shanghai 200433, China

J. Ni, Prof. H. Xiang  
Collaborative Innovation Center of Advanced Microstructures  
Nanjing 210093, China

Prof. P. Yu  
Collaborative Innovation Center of Quantum Matter  
Beijing 100084, China

Prof. P. Yu  
RIKEN Center for Emergent Matter Science (CEMS)  
Wako 351-198, Japan

The ORCID identification number(s) for the author(s) of this article can be found under <https://doi.org/10.1002/adma.201703628>.

DOI: 10.1002/adma.201703628

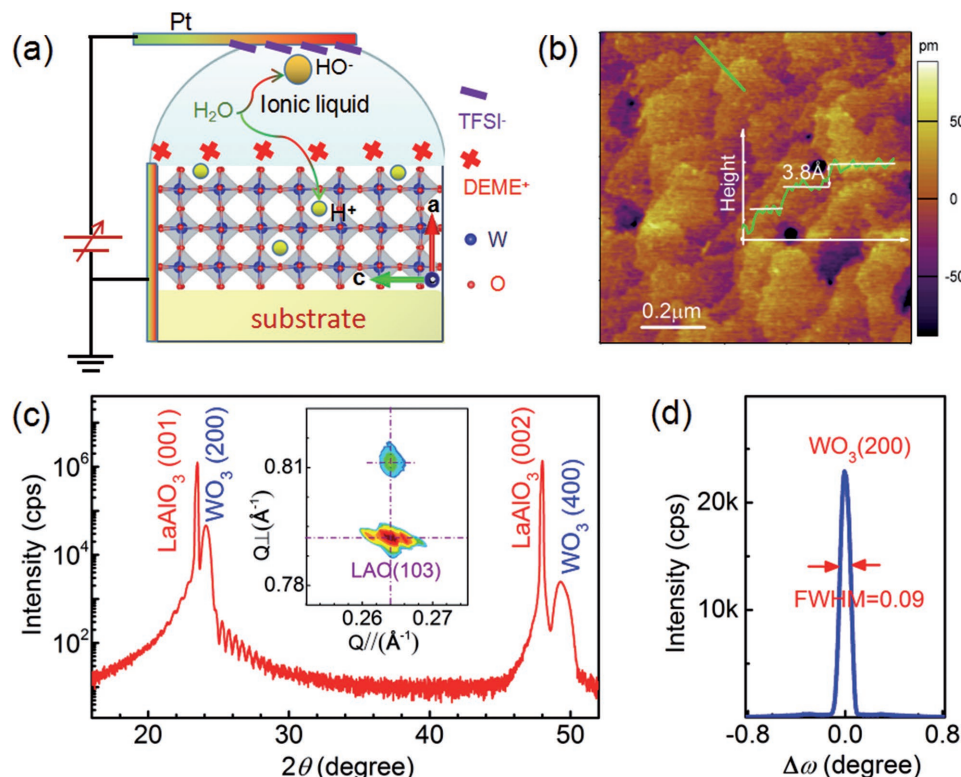


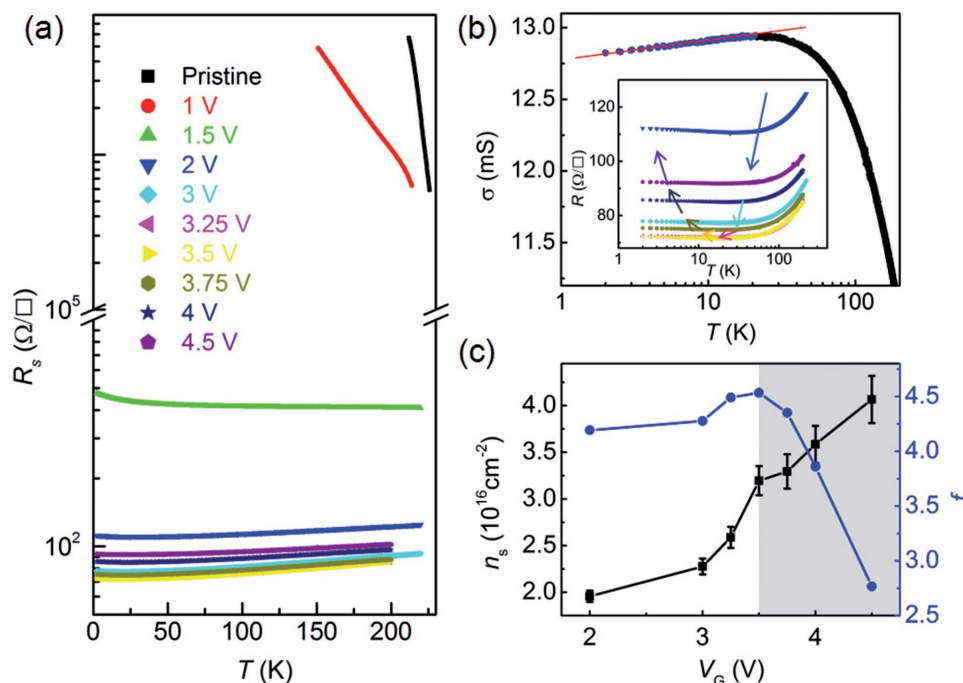
**Figure 1.** Schematic illustration of the device configuration and the structural characterizations. a) Schematic illustration of the device geometry for the ionic-liquid-gating experiment. The electric field not only induces the redistribution of the  $(\text{DEME})^+$  and  $(\text{TFSI})^-$  ions at the  $\text{WO}_3$  surface, but also leads to the electrolysis of  $\text{H}_2\text{O}$  molecules inside the ionic liquid. Consequently, the positive gating voltage leads to the intercalation of the positively charged  $\text{H}^+$  ions into the film. b) Surface topography of typical as-grown  $\text{WO}_3$  films obtained with the atomic force microscopy. Inset shows the height profile along the green line with an atomic terrace of  $\approx 3.8 \text{ \AA}$ . c)  $2\theta$ - $\omega$  scan of typical  $\text{WO}_3$  thin film grown on  $\text{LaAlO}_3$  (001) substrate. Inset is the reciprocal space mapping (RSM) result around  $\text{WO}_3$  (602)<sub>o</sub> and  $\text{LaAlO}_3$  (103)<sub>c</sub> peaks. d) Rocking curve around the  $\text{WO}_3$  (200) peak. The full width at half maximum (FWHM) is about  $0.09^\circ$ , which is close to that of the substrate used ( $\approx 0.04^\circ$ ).

deformation which has been attributed to either the electrostatic charge doping effect or oxygen ion evolution,<sup>[7,16]</sup> here we show an intrinsic ILG-induced protonation in  $\text{WO}_3$  films accompanied with a totally distinct electrical and structural phase transformations. Moreover, in contrast to the contradiction between the small charge (or oxygen vacancy) formation and the large carrier density reported in previous studies,<sup>[7,16]</sup> we show that the hydrogen dopant concentration is in excellent consistency with the carrier density estimated from the Hall measurements.

In this study, the high-quality epitaxial  $\text{WO}_3$  thin films were deposited through pulsed laser deposition method on the cubic  $\text{LaAlO}_3$  (LAO) (001) substrate (see the Experimental Section for details). The atomic flat surface morphology of the epitaxial films (exhibiting terraces with  $3.8 \text{ \AA}$  steps shown in Figure 1b) confirms the well-controlled high quality growth of the thin films. Knowing that the bulk  $\text{WO}_3$  is monoclinic at room temperature<sup>[23]</sup> and then becomes orthorhombic and tetragonal at high temperatures because of the displacement of W and the rotation of  $\text{WO}_6$  octahedra,<sup>[20,23]</sup> our epitaxial  $\text{WO}_3$  film exhibits tetragonal-like single phase, as shown in Figure 1c. Furthermore, the reciprocal space mapping (inset of Figure 1c) further suggests that the in-plane lattice of  $\text{WO}_3$  thin film is coherently locked with that of the substrates with its bulk orthorhombic  $a$  axis along the substrate (001) direction. The strained thin films

remain excellent crystalline quality as indicated by its small rocking curve (Figure 1d). In addition, the out-of-plane lattice parameter ( $D_{\text{oop}} \approx 7.38 \text{ \AA}$ ) and the thickness of films can be determined from the XRD diffraction peaks and their associated Kiessig thickness fringes.

To investigate the ILG-induced insulator-to-metal transition as well as structural transformation, a series of IL gating devices (as shown in Figure 1a) were fabricated for both the transport and in situ XRD measurements, respectively. During the study, a typical ionic liquid,  $N,N$ -diethyl- $N$ -(2-methoxyethyl)- $N$ -methylammonium bis-trifluoromethylsulfonyl-imide (DEME-TFSI), was used as the electrolyte-gating material, and the gating voltage ( $V_G$ ) was applied and changed at room temperature.<sup>[24]</sup> Figure 2a shows the temperature ( $T$ ) dependent sheet resistance ( $R_s$ ) of  $\text{WO}_3$  thin film (20 nm) measured with different  $V_G$ . Although the pristine  $\text{WO}_3$  film shows typical insulator (black line) behavior, the film resistance decreases gradually with increase of the  $V_G$ , and the IMT occurs with the gating voltage  $V_G$  of 1.5 V, which is consistent with the previous work.<sup>[16]</sup> However, with further increasing the  $V_G$  beyond the threshold value of  $\approx 3.5 \text{ V}$ , the resistance shows a surprising increase as shown in the inset of Figure 2b, which is distinct from previous studies in the same systems.<sup>[7,16]</sup> In contrast to the anomalous reverse of the resistivity, the electron carrier density  $n_s$  obtained from Hall measurements (Figure 2c and



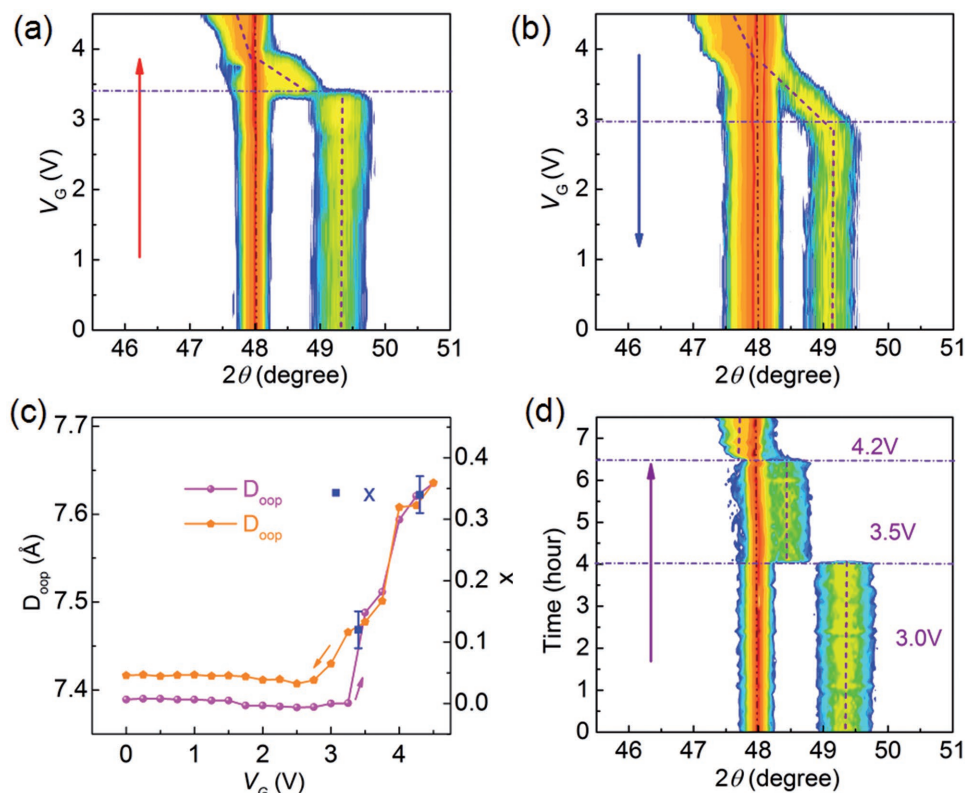
**Figure 2.** Electrical transport properties of  $\text{WO}_3$  thin films. a) Temperature-dependent sheet resistance measured at different gating voltages ( $V_G$ ). b) Log  $T$  plot of sheet conductance with  $V_G = 3.0$  V. The red line is a linear fitting at the low temperature region (blue dots). The inset shows the close-view of curves with  $V_G$  from 2.0 to 4.5 V. The arrows, dyed the same colors with  $R(T)$  curves in (a), indicate the trend of resistance modulation with increasing of gating voltages. c) Carrier density  $n_s$  (measured at 2 K) and fitting parameter  $f$  as a function of  $V_G$ . The gray region is guide to the eyes. The film thickness is 20 nm.

Figure S1a, Supporting Information) increases continuously as  $V_G$  increases. Besides, an upturn emerges at low temperature region for all  $R(T)$  curves in the metallic state, as shown in the log( $T$ ) plot of sheet resistance (the inset of Figure 2b), which can be likely attributed to the weak localization (WL), as supported by the nice fitting of the low temperature dependent sheet conductivity with the WL model (red line in Figure 2b).<sup>[25]</sup> Moreover, a positive magnetoresistance (Figure S1b, Supporting Information) suggests both spin–orbital coupling and electron–electron interaction are strong in the WL states.<sup>[25–27]</sup> In the 2D model, the correction to the conductivity at zero field is given by  $\Delta\sigma(T) = f \frac{e^2}{\pi h} \ln\left(\frac{T}{T_0}\right)$ , where  $T_0$  is a reference temperature related to the transport mean free path and the factor  $f$  is related to the mechanism of backscattering collisions, which changes for different dominating collisions (electron–electron, electron–phonon, and strong Coulomb interaction).<sup>[25]</sup> As shown in Figure 2c,  $f$  changes slightly with increasing  $V_G$  up to 3.5 V, while decreases rapidly as further increasing  $V_G$ . The anomalous behaviors of  $R$  and  $f$  indicate an intriguing phase transformation with  $V_G$  around 3.5 V.

To obtain further insights into the mechanism of this novel-conducting behavior, we have performed a series of in situ XRD measurements during the ILG, as summarized in Figure 3a. The  $2\theta$ – $\omega$  scans around  $\text{WO}_3$  (400) peak show no obvious shift of the peak position with  $V_G$  up to 3.5 V. While with further increase of the  $V_G$ , the peak gradually shifts to the left, suggesting a clear enhancement of the out-of-plane lattice constant. By reversing the  $V_G$  down to 0 V with the same step,

the diffraction peak nearly returns to the original position with a slightly offset (Figure 3b). It is worth noting that regardless of the applied  $V_G$ , the in-plane lattice parameter ( $D_{ip}$ ) is strongly strained with that of the LAO (001) substrate without strain relaxation (Figure S2, Supporting Information). This result suggests that the ILG has little influence on the crystalline quality of the thin films during the phase transformation. Calculated from the XRD results, the structural phase transformation leads to continue the increase of  $D_{oop}$  from 7.38 Å (pristine) to 7.64 Å (as shown in Figure 3c), with the chemical expansion of  $\approx 3.5\%$ . Thus, combining both the transport and structural measurements, we can readily define a threshold voltage, above which the film undergoes a structural phase transformation with the anomalous change of transport properties. To further clarify this point, we measured the time dependence of ILG at fixed  $V_G$  via continuous  $2\theta$ – $\omega$  scans. As shown in Figure 3d, the diffraction peak remained unchanged at a fixed  $V_G$  of 3 V for 4 h, but changed rapidly (within a few minutes) into a new structural state for  $V_G$  of 3.5 V, then remained stable until a higher voltage was applied. These results strongly suggest that the structural transformation is dominated by the value of  $V_G$ , rather than the gating duration. Thus, the corresponding electronic state can be well tuned with the programed gating voltages in a reversible and reproducible manner (as shown in Figure S3 of the Supporting Information).

It has been reported that the crystal structure of  $\text{WO}_3$  film is easily distorted due to varying of carrier density or ion intercalation.<sup>[20–22]</sup> However, the phase transition induced by charge accumulation is usually discontinuous,<sup>[7,20]</sup> which is



**Figure 3.** Structural evolution of WO<sub>3</sub> thin films during the ionic-liquid gating. In situ 2θ-ω scans of 20-nm-thick WO<sub>3</sub> thin film with a) increasing of V<sub>G</sub> and b) decreasing of V<sub>G</sub>, respectively. The curves were obtained at every 0.25 V interval and with 15 min dwell time before each scan. c) Gating-voltage (V<sub>G</sub>) dependence of the lattice parameter (D<sub>oop</sub>) for a 20-nm-thick WO<sub>3</sub> film and its estimated H-dopant concentration (x, blue squares) according to the chemical expansion.<sup>[28]</sup> The arrows indicate the gating-voltage-sweeping directions. d) Time dependent 2θ-ω scans of 20-nm-thick WO<sub>3</sub> thin film at different V<sub>G</sub>.

inconsistent with our observation of a wide range of continuous structural deformation. Furthermore, the sheet carrier density (in the order of 10<sup>16</sup> cm<sup>-2</sup> estimated from the Hall measurement) is dramatically larger than the typical charge modulation through the ILG-induced electrostatic gating (≈10<sup>15</sup> cm<sup>-2</sup>). Besides, the sample remains in an intermediate resistant state (Figure S1c, Supporting Information) when turning off the gating voltage, while the resistance would recover back to the pristine insulating state rapidly if the electrostatic gating plays the essential role. Moreover, when removing the ILG and then capping the film with a thin layer of Au to isolate the air, the structure remains in an intermediate state instead of returning back to the pristine state even for several days (Figure 4a), which confirms that the electrostatic gating is not the case for our results. With this discussion, we are confident to assign the electrochemically driven ion migration as the main mechanism for the discovered insulator-to-metal transition as well as the large and continuous structural transformation.

It has been reported that the ILG can induce both oxygen ion extraction or hydrogen ion intercalation in the materials with a positive bias V<sub>G</sub>.<sup>[14–18]</sup> However, the observed electrical and structural transformation in the current studies is dramatically different from the previously reported observations of ILG modulated WO<sub>3</sub> through the oxygen ion evolution.<sup>[16]</sup> Indeed, energy dispersive spectroscopy measurements were

carried out on samples in both intermediate and pristine states, which show no obvious variation of the oxygen concentration through the ILG (Figure S4, Supporting Information). To get more direct information about the oxygen and hydrogen concentrations in the ILG-induced metallic state, the depth profile SIMS measurements were performed on a series of films gated at different environments and V<sub>G</sub>, together with the pristine sample as reference. To trace the oxygen evolution during the ILG, we prepared a sample gated with 4.5 V for 4 h and then relaxed back the initial state in high purity of <sup>18</sup>O<sub>2</sub> environment. If the oxygen evolution plays an essential role during the ILG, a large amount of <sup>18</sup>O ions will be accumulated into the sample during the structural relaxation process by intercalating the <sup>18</sup>O ions from the environment.<sup>[14]</sup> However, as comparing with the pristine sample, the <sup>18</sup>O concentration in the gated sample (as shown in Figure 4b) remains almost unchanged, close with that in the nature oxygen gas. These results clearly suggest that the oxygen evolution is not the essential factor for the phase transformation.

Instead, we tentatively attribute this to the hydrogen evolution during the ILG. To prove this, we carried out the hydrogen depth profiles measurement through SIMS on a series of controlling samples, as shown in Figure 4c. Before the measurements, all samples were capped by 5 nm thick Au to maintain the gated sample in the intermediate state. As shown in Figure 4c, obvious hydrogen signals were observed in both



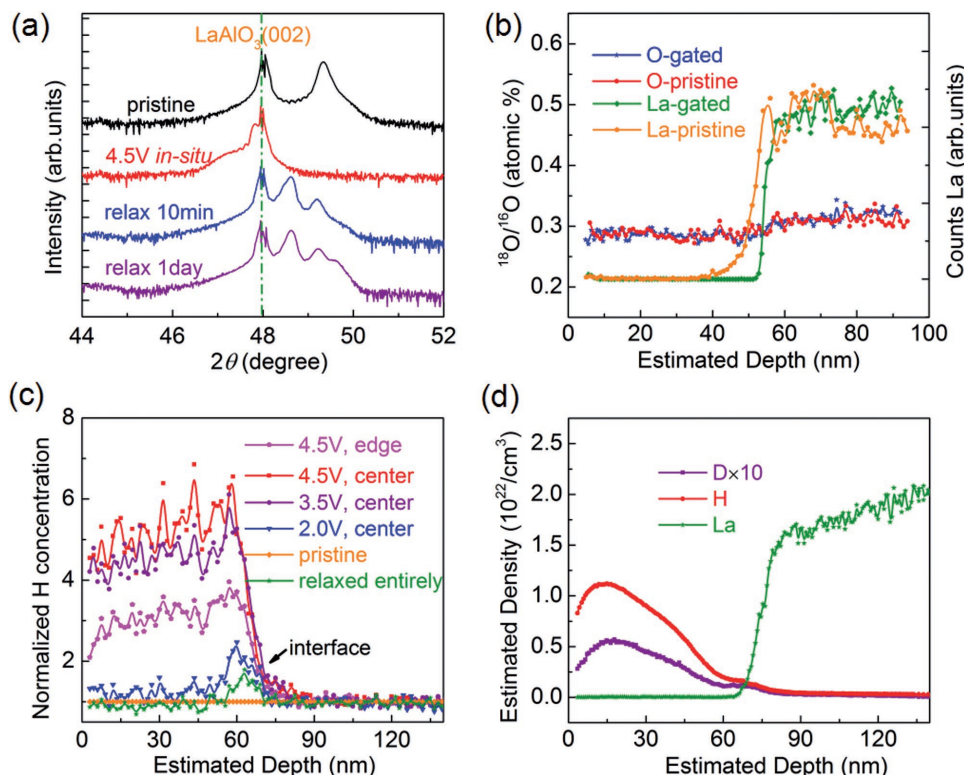


**Figure 4.** Structural and compositional characterizations for samples at representative states. a)  $2\theta$ - $\omega$  scans of 60-nm-thick  $\text{WO}_3$  films at different states. The relaxed sample was capped with 10 nm Au immediately after removing IL. b) Depth profiles of  $^{18}\text{O}$  ion in a sample gated at 4.5 V and then relaxed back to the initial state within  $^{18}\text{O}_2$  environment together with a pristine (as-grown) sample. The La signal can be taken as a marker for the position of the interface. c) Depth profiles of the H ion in a series of  $\text{WO}_3$  samples treated in different manners. All data are normalized by the background signal of the pristine sample (orange). The magenta data were obtained at the edge of the sample gated at 4.5 V, while all the others were measured at the center of the samples. The relaxed sample (olive) represents the film placed in air at room temperature for 72 h after gating at 4.5 V. d) Quantitative depth profiles of H and D concentrations in a sample gated at 4.5 V. The gating time was set to be 4 h for all gating measurements here, which is sufficient to reach the equilibrium state during the gating. All films, except the relaxed sample, are capped with 5 nm Au layer before SIMS measurements.

samples gated at  $V_G = 3.5$  and 4.5 V, in which the structural transformation occurs. Furthermore, the hydrogen distributes throughout the film thickness, suggesting that the electrochemical reaction is involved in the entire film during ILG. On the other hand, the hydrogen signals in pristine sample and the samples show clearly IMT but without the appearance of structural transformation ( $V_G = 2$  V) are only comparable to that of the substrate. Besides, a relaxed sample, which had been placed in the air for 72 h without capping after gating at 4.5 V for 4 h, shows undetectable hydrogen signal as well, suggesting the occurrence of hydrogen extraction after the gating. Accordingly, the emergence of additional peak in XRD patterns measured in relaxed sample (Figure 4a) can be ascribed as the phase separation caused by nonuniform distribution of the hydrogen. Indeed, the hydrogen concentration at the edge of the sample gated at  $V_G = 4.5$  V decreases dramatically as compared with that at the center and the nonuniform depth distribution is also observed (Figure 4d). These results clearly suggest that the large continuous structural transformation of  $\text{WO}_3$  film can be mainly attributed to the hydrogen intercalation through the ILG.

Above the threshold voltage for hydrogen injection ( $\approx 3.5$  V), the hydrogen concentration increases with further increasing of  $V_G$ , suggesting that the migration of hydrogen can be

modulated continuously by the  $V_G$ , which is also consistent with the close correlation between the continuous lattice expansion with increasing of  $V_G$ . In addition, the quantitative SIMS analysis (Figure 4d) shows that the hydrogen concentration is about  $1 \times 10^{22} \text{ cm}^{-3}$  (0.5 hydrogen atom per formula unit cell) for the intermediate state, which is quantitatively consistent with the carrier density obtained through the Hall effect measurement in the sample gated with  $V_G = 3.5$  V state (the surface density of  $3 \times 10^{16} \text{ cm}^{-2}$  as shown in Figure 2c for the 20 nm film corresponds to the bulk carrier density of  $1.5 \times 10^{22} \text{ cm}^{-3}$ ). We note that the previous studies on protonated bulk  $\text{WO}_3$  show a clear correlation between the hydrogen concentration and the volume expansion.<sup>[28]</sup> Accordingly, we can further estimate the hydrogen content in our gated samples from its crystalline volume, which is about 0.1 and 0.35 hydrogen atom per formula unit cell for the samples gated with 3.5 and 4.5 V, respectively. The slight difference between the SIMS measurement and the estimation can be attributed to the different strain and quality between our thin films and referenced polycrystalline samples.

In order to trace the origin of hydrogen ions in the gated  $\text{WO}_3$ , we doped the ionic liquid with heavy water ( $\text{D}_2\text{O}$ ) before ILG and found clear deuterium signal in the gated  $\text{WO}_3$  (Figure 4d), which provides solid evidence to attribute the origin of

hydrogen ions to the water content inside the ionic liquid, which is consistent with our previous studies in SrCoO<sub>2.5</sub> system.<sup>[18]</sup> We note that the water content inevitably exists in the as-received ionic liquid, and our estimation shows that the water concentration (typically in the order of ppm) inside the ionic liquid is more than sufficient to provide enough hydrogen for the ILG-induced phase transformation.

We note that similar result has also been reported earlier that the hydrogen adsorption can be realized at the interface of ZnO and ionic liquid, due to dissociation of H<sub>2</sub>O into proton and hydroxyl under a threshold  $V_G$  of  $\approx 1.5$  V. And this effect can provide the density of H<sup>+</sup> up to  $10^{17}$  cm<sup>-2</sup>.<sup>[29]</sup> In our current study, with  $V_G$  around 1.5 V, the positively charged H<sup>+</sup> ions hydrolyzed from water will accumulate first at the surface of WO<sub>3</sub> films. In this case, the adsorbed H<sup>+</sup> ions at the sample surface will lead to extraordinarily large carrier density modulation and result in the insulator-to-metal transition, similarly as the case of the IL gated ZnO.<sup>[29]</sup> With further increasing of  $V_G$ , the concentration of adsorbed hydrogen increases accordingly, which results in the further decrease of resistivity as well as increase of carrier density. However, due to the large energy barrier, the H<sup>+</sup> intercalation is only confined within the top surface layers of the samples, and cannot trigger the structural modification in the bulk form. However, with the  $V_G$  above 3.5 V, the overpotential across the film surface becomes high enough to overcome the potential barrier for the ionic diffusion, the H<sup>+</sup> ions will diffuse into the whole films. Meanwhile, the extensive vacancy channels in WO<sub>3</sub> facilitate the subsequent hydrogen migration among the entire film, resulting in the experimentally observed continuous structural transformations with expanded out-of-plane lattice constant.

To shed more light on the intriguing properties of the protonated WO<sub>3</sub>, we have performed first principle calculations. The studies show that the doped hydrogen atoms prefer to bond together with the oxygen ions in the octahedral corner of the protonated WO<sub>3</sub> (Figure S5, Supporting Information), leading to the lattice expansion along the increase of hydrogen concentration (Table S1, Supporting Information). For instance, for H<sub>0.375</sub>WO<sub>3</sub>, the out of plane lattice constant is expanded by  $\approx 4.1\%$  (from 7.380 to 7.683 Å), which is well consistent with our experimental observations ( $\approx 3.4\%$  for H<sub>0.35</sub>WO<sub>3</sub>). The comparison of the calculated density of states (DOS) for WO<sub>3</sub> and protonated WO<sub>3</sub> provides clearly evidence for the protonation-induced insulator-to-metal transition, as shown in Figure S6 (Supporting Information). The results reveal that the pristine WO<sub>3</sub> is a band insulator with well-defined band gap, while the protonated WO<sub>3</sub> samples show notably DOS at Fermi level, confirming the metallic nature of the protonated samples. Furthermore, since there are multiple equilibrium binding sites for the hydrogen atoms within the lattice, it would be natural to expect the protonated sample to have notably disordered hydrogen ions. Thus, we can naturally attribute the slight suppression of the metallization to the enhancement of disorder upon hydrogen intercalation.

Although protonated WO<sub>3</sub> has been widely studied through photochemical, electrochemical, and catalytic methods in the last several decades with the discovery of protonation-induced insulator-to-metal transition as well as the structural transformation,<sup>[27,28,30–32]</sup> our ILG study offers a readily pathway to

control the electrical and structural phase transformation in WO<sub>3</sub> in a reversible and continuous manner. The discovery shows promising application in the practical electrical and optical devices, due to its excellent accessibility and tunability in contrast to other electrochemical methods.

In summary, we have realized an ILG-induced hydrogen evolution and its associated phase transformation in the high-quality single crystal WO<sub>3</sub> thin films. The hydrogen evolution can be modulated continuously by the gating voltage, leading to the evolution of structural phase transformation and manipulation of the electronic transport properties, in a distinct fashion from the electrostatic charge accumulation and oxygen ionic migration. This study identifies the ILG-induced hydrogen evolution as a generic tuning knob to engineering the material functionalities, and we envision that this approach can be readily extended to a large group of material systems with the discovery of novel crystalline structures and exotic electronic states.

## Experimental Section

**Thin Film Fabrication:** WO<sub>3</sub> thin films were deposited on LAO (001) substrate by a home designed pulsed laser deposition system. The O<sub>2</sub> pressure was controlled to be 0.1 mbar and the deposited temperature was 680 °C. The energy density of pulsed laser (wavelength  $\lambda = 248$  nm) was around 0.5 J cm<sup>-2</sup> and the frequency was 3 Hz. After the deposition, samples were cooled down to room temperature in 1 mbar of O<sub>2</sub> with the cooling rate of 5 °C min<sup>-1</sup>.

**In Situ Transport and XRD Measurements:** Hall bar device structure with the dimension of 3 mm  $\times$  1 mm was employed for the transport measurements. 20 nm Au layer was deposited on the WO<sub>3</sub> thin films as the gate electrode by ion-beam sputtering, and a screwed Pt wire was selected as the counter electrode. Samples were placed in a small quartz-bowl and covered entirely by the ionic liquid. Resistance was measured by a Quantum Design DynaCool system through four probe electrical contact geometry to eliminate the influence of contact resistance. The source-drain current was set to 1  $\mu$ A (DC) for all measurements. For every gating voltage, the voltage was applied at the room temperature with air environment, and after waiting for 30 min, the chamber was cooled down to 240 K and then pumped to vacuum. For in situ XRD measurements, two contact electrodes were made on the opposite edges of samples, and a screwed Pt wire was put nearby as the counter electrode. Then the whole gating device was put on the XRD sample-holder. The  $2\theta$ - $\omega$  and reciprocal space mapping of in situ XRD measurement were performed in air and at room temperature, with a high-resolution diffractometer (Smartlab, Rigaku) using monochromatic Cu K $\alpha_1$  radiation ( $\lambda = 1.5406$  Å). The thickness of the IL was carefully controlled so as to get strong enough diffracted X-ray signal. The  $V_G$  dependent  $2\theta$ - $\omega$  scans were measured with the step of 0.25 V, and the time interval for each curve was set to 15 min.

**Secondary Ion Mass Spectroscopy Measurements:** SIMS measurements for H and <sup>18</sup>O were carried out using a TOF.SIMS 5-10 instrument (IONTOF GmbH). The sputtering area was 350  $\mu$ m  $\times$  350  $\mu$ m and the detecting area was 150  $\mu$ m  $\times$  150  $\mu$ m in order to avoid the disturbance from the crater edge. The interface position was indexed through the measurements of the W, La, and Al elements, while the H (or <sup>18</sup>O and <sup>16</sup>O) signal was recorded simultaneously. All samples were measured under the same conditions, and the H<sup>+</sup> signals were normalized by the background signal in the substrate. The quantitative H and D analysis was carried out on a SIMS instrument (ADEPT 1010), during which the sputtering area was 126.5  $\mu$ m  $\times$  126.5  $\mu$ m and the detecting area was 50  $\mu$ m  $\times$  50  $\mu$ m. The concentration of H (D) was calculated by profiling H (D)-implanted SiO<sub>2</sub> with known hydrogen dosage.

**Density Functional Theory (DFT) Calculation:** DFT calculations on WO<sub>3</sub> and H<sub>x</sub>WO<sub>3</sub> were performed on the basis of the projector augmented

wave method encoded in the Vienna ab initio simulation package.<sup>[33–36]</sup> The exchange–correlation potential is treated by PBEsol and the plane wave cutoff energy is set to 500 eV.<sup>[37]</sup> We use a  $6 \times 6 \times 6$  Monkhorst-Pack  $k$ -point mesh for the 32-atoms unit cell of  $\text{WO}_3$ . During the simulation, all the atoms are allowed to relax until the atomic forces are smaller than  $0.02 \text{ eV } \text{\AA}^{-1}$ . The in-plane lattice constants are fixed to that ( $7.58 \text{ \AA}$ ) of the substrate adopted in the experiment, while the out-of-plane lattice constant is fully optimized.

## Supporting Information

Supporting Information is available from the Wiley Online Library or from the author.

## Acknowledgements

M.W. and S.S. contributed equally to this work. The study was financially supported by the National Basic Research Program of China (2015CB921700, 2016YFA0301004) and Initiative Research Projects of Tsinghua University (20141081116).

## Conflict of Interest

The authors declare no conflict of interest.

## Keywords

hydrogen evolution, ionic-liquid gating, phase transformation,  $\text{WO}_3$

Received: June 29, 2017  
Revised: August 30, 2017  
Published online: October 23, 2017

- [1] R. Kötzt, M. Carlen, *Electrochim. Acta* **2000**, 45, 2483.
- [2] A. S. Dhoot, C. Israel, X. Moya, N. D. Mathur, R. H. Friend, *Phys. Rev. Lett.* **2009**, 102, 136402.
- [3] R. Scherwitzl, P. Zubko, I. G. Lezama, S. Ono, A. F. Morpurgo, G. Catalan, J. M. Triscone, *Adv. Mater.* **2010**, 22, 5517.
- [4] M. Nakano, K. Shibuya, D. Okuyama, T. Hatano, S. Ono, M. Kawasaki, Y. Iwasa, Y. Tokura, *Nature* **2012**, 487, 459.
- [5] D. Braga, I. G. Lezama, H. Berger, A. F. Morpurgo, *Nano Lett.* **2012**, 12, 5218.
- [6] X. Meng, F. Quenneville, F. Venne, E. D. Mauro, D. Işık, M. Barbosa, Y. Drolet, M. M. Natile, D. Rochefort, F. Soavi, C. Santato, *J. Phys. Chem. C* **2015**, 119, 21732.
- [7] S. Nishihaya, M. Uchida, Y. Kozuka, Y. Iwasa, M. Kawasaki, *ACS Appl. Mater. Interfaces* **2016**, 8, 22330.
- [8] K. Ueno, S. Nakamura, H. Shimotani, A. Ohtomo, N. Kimura, T. Nojima, H. Aoki, Y. Iwasa, M. Kawasaki, *Nat. Mater.* **2008**, 7, 855.
- [9] A. S. Dhoot, S. C. Wimbush, T. Benseman, J. L. MacManus-Driscoll, J. R. Cooper, R. H. Friend, *Adv. Mater.* **2010**, 22, 2529.
- [10] Y. Lee, C. Clement, J. Hellerstedt, J. Kinney, L. Kinnischtzke, X. Leng, S. D. Snyder, A. M. Goldman, *Phys. Rev. Lett.* **2011**, 106, 136809.
- [11] J. T. Ye, Y. J. Zhang, R. Akashi, M. S. Bahramy, R. Arita, Y. Iwasa, *Science* **2012**, 338, 1193.
- [12] A. T. Bollinger, G. Dubuis, J. Yoon, D. Pavuna, J. Misewich, I. Božović, *Nature* **2011**, 472, 485.
- [13] Y. Yamada, K. Ueno, T. Fukumura, H. T. Yuan, H. Shimotani, Y. Iwasa, L. Gu, S. Tsukimoto, Y. Ikuhara, M. Kawasaki, *Science* **2011**, 332, 1065.
- [14] J. Jeong, N. Aetukuri, T. Graf, T. D. Schladt, M. G. Samant, S. S. P. Parkin, *Science* **2013**, 339, 1402.
- [15] J. Jeong, N. B. Aetukuri, D. Passarello, S. D. Conradson, M. G. Samant, S. S. P. Parkin, *Proc. Natl. Acad. Sci. USA* **2015**, 112, 1013.
- [16] S. G. Altendorf, J. Jeong, D. Passarello, N. B. Aetukuri, M. G. Samant, S. S. P. Parkin, *Adv. Mater.* **2016**, 28, 5284.
- [17] K. Shibuya, A. Sawa, *Adv. Electron. Mater.* **2016**, 2, 1500131.
- [18] N. Lu, P. Zhang, Q. Zhang, R. Qiao, Q. He, H. Li, Y. Wang, J. Guo, D. Zhang, Z. Duan, Z. Li, M. Wang, S. Yang, M. Yan, E. Arenholz, S. Zhou, W. Yang, L. Gu, C. W. Nan, J. Wu, Y. Tokura, P. Yu, *Nature* **2017**, 546, 124.
- [19] A. Hjelm, C. G. Granqvist, J. M. Wills, *Phys. Rev. B* **1996**, 54, 2436.
- [20] A. D. Walkingshaw, N. A. Spaldin, E. Artacho, *Phys. Rev. B* **2004**, 70, 165110.
- [21] N. Haldolaarachchige, Q. Gibson, J. Krizan, R. J. Cava, *Phys. Rev. B* **2014**, 89, 104520.
- [22] D. Hirai, E. Climent-Pascual, R. J. Cava, *Phys. Rev. B* **2011**, 84, 174519.
- [23] E. Salje, K. Viswanathan, *Acta Cryst.* **1975**, A31, 356.
- [24] R. Misra, M. McCarthy, A. F. Hebard, *Appl. Phys. Lett.* **2007**, 90, 052905.
- [25] P. A. Lee, T. V. Ramakrishnan, *Rev. Mod. Phys.* **1985**, 57, 287.
- [26] J. Chen, H. J. Qin, F. Yang, J. Liu, T. Guan, F. M. Qu, G. H. Zhang, J. R. Shi, X. C. Xie, C. L. Yang, K. H. Wu, Y. Q. Li, L. Lu, *Phys. Rev. Lett.* **2010**, 105, 176602.
- [27] U. Tritthart, A. Gavriluk, W. Gey, *Czech. J. Phys.* **1996**, 46, 2495.
- [28] R. H. Jarman, P. G. Dickens, *J. Electrochem. Soc.: Solid State Sci. Technol.* **1982**, 129, 2276.
- [29] H. Yuan, H. Shimotani, A. Tsukazaki, A. Ohtomo, M. Kawasaki, Y. Iwasa, *J. Am. Chem. Soc.* **2010**, 132, 6672.
- [30] R. S. Crandall, B. W. Faughnan, *Appl. Phys. Lett.* **1976**, 28, 95.
- [31] B. S. Hobbs, A. C. C. Tseung, *J. Electrochem. Soc.* **1972**, 119, 580.
- [32] R. S. Crandall, B. W. Faughnan, *Phys. Rev. Lett.* **1977**, 39, 232.
- [33] P. E. Blöchl, *Phys. Rev. B* **1994**, 50, 17953.
- [34] G. Kresse, D. Joubert, *Phys. Rev. B* **1999**, 59, 1758.
- [35] G. Kresse, J. Furthmüller, *Comput. Mater. Sci.* **1996**, 6, 15.
- [36] G. Kresse, J. Furthmüller, *Phys. Rev. B* **1996**, 54, 11169.
- [37] J. P. Perdew, K. Burke, M. Ernzerhof, *Phys. Rev. Lett.* **1996**, 77, 3865.